Size effect in plasmonic-enhanced photocatalysis in Au/TiO 2 nanocomposites

Chawki Awada, Mohammed Benali Kanoun, Faheem Ahmed, Osama Saber, Aya Osama, Mostafa Osama, Christian Jonin, Pierre-François Brevet

▶ To cite this version:

Chawki Awada, Mohammed Benali Kanoun, Faheem Ahmed, Osama Saber, Aya Osama, et al.. Size effect in plasmonic-enhanced photocatalysis in Au/TiO 2 nanocomposites. Optical Materials, 2025, ⟨10.1016/j.optmat.2025.117293⟩. ⟨hal-05139815⟩

HAL Id: hal-05139815
https://hal.science/hal-05139815v1

Submitted on 2 Jul 2025

Size effect in plasmonic-enhanced photocatalysis in Au/TiO_2 nanocomposites

Chawki Awada[1]*, Mohammed Benali Kanoun[2], Faheem Ahmed[3], Osama Saber[1], Aya Osama[1], Mostafa Osama[1], Christian Jonin[4], Pierre-François Brevet[5].

[1]Department of Physics, College of Science, King Faisal University, P.O. Box 400, Al-Ahsa 31982, Saudi Arabia

[2]Department of Mathematics and Sciences, College of Humanities and Sciences, Prince Sultan University, P.O. Box 66833, Riyadh, 11586, Saudi Arabia

[3]Department of Applied Sciences & Humanities, Faculty of Engineering & Technology, Jamia Millia Islamia (Central University), New Delhi-110025, India

[4]Laboratoire Charles Coulomb, Université de Montpellier, UMR 5221 CNRS, Montpellier 34095, France.

[5]Institut Lumière Matière, Université de Lyon, UMR 5306 CNRS, Université Claude Bernard Lyon 1, CEDEX 69622 Villeurbanne, France

Corresponding author: cawada@kfu.edu.sa

Abstract

One of the important challenges encountered in photocatalysis applications is to fabricate high performance photocatalysts with an easy and low-cost fabrication method and sustaining a slow hole-electron recombination rate. The latter can be achieved by promoting the synergetic effect between noble metals and metal oxides such as titanium oxide (TiO_2). In this work, gold nanostars/TiO_2 (GNS/TiO_2) nanocomposites were prepared using the impregnation method. A study of the dependence of the size on the synergetic effect of GNS/TiO_2 nanocomposites was investigated using TiO_2 nanoparticles with an average size of 5 nm and 20 nm, respectively. The structural, morphological, elemental and optical properties of GNS/TiO_2 nanocomposites were studied by X-ray diffraction (XRD), High-resolution transmission electron microcopy (HRTEM), Energy dispersion X-ray (EDX), selected area electron diffraction (SAED), Raman spectroscopy, adsorption/desorption isotherm, and UV-Vis optical spectroscopy techniques. The photocurrent study was performed with different films of GNS/TiO_2 nanocomposites indicating the importance of the size to enhance photocurrents with the presence of GNS. The photocatalytic activity of the prepared nanocomposites was studied toward the photodegradation of the Naphthol Green B complex dye. 5 nm and 20 nm pure anatase TiO_2 exhibited a very fast degradation of the dye during 19 and 70 minutes with kinetics reaction rate of 0.078 and 0.03 min^{-1} respectively. By adding GNS, 5 nm and 20 nm GNS/TiO_2 showed shorter photodegradation time of 10 and 15 minutes with kinetics reaction rate of 0.241 and 0.155 min^{-1} respectively. The latter confirms the strong synergetic effect between GNS and 5nm TiO_2 that may come from its smaller size compared to the 20 nm TiO_2 nanocomposite system. The first principal calculations were performed to study the stability and electronic structures of the Au/TiO_2 composite interface. The interfacial charge properties and the potential drop between the gold and TiO_2 were also studied. The adsorption energies of the Naphthol Green B on the Au/TiO_2 composite interface were also examined.

Keywords: GNS/TiO_2, photocatalysis, synergetic, plasmonic, interfacial charge, adsorption energy

Introduction

Over the last decades, TiO_2 nanoparticles loaded with noble metal metallic nanoparticles possessing a localized surface plasmon resonance (LSPR) have been used for photocatalytic reactions within the visible optical spectrum[1–6]. As a result, plasmonic metal nanoparticles doped semiconductor nanostructures have improved efficiency for water splitting, decomposition of organic compounds or photovoltaic devices by 10–15%[7–10]. Noble metals such as Pt, Au, Ag or Pd have been used for visible–light activation, all increasing the photocatalytic activity of TiO_2[11–15].

Plasmonics nanostructures, i.e. metallic nanostructures possessing the collective excitation of the conduction band electrons when interacting with light, have received a lot of attention and have brought to the field extensive progress due to the amelioration of the fabrication technologies. In particular, the down-sizing of metallic nanostructures can confine the excited conduction band electrons, thereby inducing large amplification of the electric field in the vicinity of the nanostructures and the control of the geometrical aspect of the nanostructures has promoted a great control over these (LSPR) collective excitations [16–18]. When molecules or semiconductors are close to these metallic nanostructures, electron transfer can be achieved with great efficiency from the metal as it can be the case with TiO_2 [19–21]. Other semiconducting metal oxides, e.g. $BiFO_3$, $SrTiO_3$ also showed an increase in their efficiency after loading them with noble metal nanoparticles [22–28]. The injection of electrons from the semiconductors can be induced through different ways such as enhanced electric field due to the excited plasmons or electron-hole generation [29–32].

Although much progress has been reported on the metal/TiO_2 nanocomposites, there are remaining challenges to overcome in relation to the plasmon resonance spectral range and amplitude. This is why using metallic nanostructures with a specific shape sustaining plasmon modes in a large visible-IR spectral range is of great interest for the enhancement of the photocatalytic activities of metal/TiO_2 nanocomposites[33,34]. Gold nanostructures with the shape of triangle pyramid, star, square cube, sphere, rod, etc… do exhibit plasmon resonance modes that can be excited at different wavelengths with the result of different orders of magnitude of enhancement[35–38]. Specifically, one of the shapes sustaining high optical enhancement with gold nanoparticles is the star (GNS). In this case, plasmon excitation with different wavelengths attributed to the spikes and the core is possible. In particular, individual hotspots generated at the spikes possess high electromagnetic enhancement playing a crucial role during the photocatalytic activation[39–41].

TiO_2 nanoparticles have remarkable physical and chemical properties that depend on their size, morphology, phase structure, crystallinity, all resulting from the synthesis process of these nanoparticles such as sol gel, solvothermal, impregnation, etc[42–47]. These properties have a great effect on the photocatalytic activity[48,49]. For instance, decreasing the size of the nanoparticles can induce a quantum confinement effect, reduce the band bending energy, reduce the charge layer and increase the surface to volume ratio [50,51]. Therefore, investigating nanocomposites where both gold and TiO_2 nanoparticles have nanometer size is important. Up to now, such a study where the size effect of the TiO_2 nanoparticles is investigated in conjunction with GNS formed by the impregnation route has not been reported although the question of gold atom doping has been investigated in a previous work [45]. In this context, the present work focuses on the size effect of two 5 nm and 20 nm diameter TiO_2 nanoparticles on the synergy with GNS for photocatalytic activity, the gold nanostars particles sustaining a high field enhancement due to the surface plasmon excitation within the visible spectrum. With the large 20 nm size nanoparticles, a crystal structure close to that of the bulk structure is expected. In detail, this work consists of two parts: first a photodegradation and a photocurrent study and second a theoretical study of the interfacial charge transfer in Au/TiO_2 nanocomposites with the adsorption energy evaluation of dyes.

Experimental details

Materials

Two types of commercial TiO_2 nanoparticles with different sizes were purchased. The first type contains nanoparticles with an average diameter of 5 nm ordered from Skyspring Nanomaterials (product ID: 7930DL), USA. The second one contains nanoparticles with an average diameter of 20 nm purchased from Sigma-Aldrich (CAS number 637254-50G), Germany. A 10 mL stock solution of 5 mM GNS dispersed in water was purchased from Nanoimmunotech Inc. (CAS NR:7440-57-5), Vigo, Spain. The GNS had an average overall diameter of approximately 50 nm.

Preparation of nanomaterials

The prepared aqueous solutions of the GNS/TiO_2 nanocomposites, called GNS/TiO_2 (5 nm) and GNS/TiO_2 (20 nm) respectively, were obtained with the dry impregnation method. Typically, 1 g of TiO_2 nanoparticles powder was impregnated with a 0.5 mM solution of the GNS. To obtain a 0.1 wt.% Au content in the final product, 10 mL of the GNS suspension was added to TiO_2 at room temperature under strong stirring, see Figure 1. The mixture was stirred for one hour and then the product was dehydrated in vacuum for 48 h. The films were fabricated using the spin coating method. 200 μL of GNS/TiO_2 nanocomposites aqueous solution with a concentration 10^{-3} M was deposited into 2 cm x 2 cm fluorine tin oxide glass substrate (FTO) with a 6000 rpm during 45 s. Raman spectroscopy was used to assure the presence of a film onto the substrate, see Figure S3. The thickness of the films was estimated to be around 300 nm using the model of Emslie.

Characterization of the prepared nanomaterials

For HRTEM (JEOL, model JEM-2100F), SAED, EDX analysis, all samples were sonicated for 10 mins. For HRTEM, 5 μL of the dispersed solution was deposited on a carbon coated copper grid. Raman spectra were collected using a confocal Raman microscope (LabRAM HR800, Horiba, France) equipped with a multichannel charge-coupled detector (CCD). An excitation source consisting of a He-Cd laser with a wavelength of 442 nm, a grating of 1800 l/mm, and 20 mW output power was used. At room temperature and in backscattering configuration, Raman spectra were measured with a spectral resolution of 0.8 cm^{-1}. The same laser was used for photoluminescence measurement but with an excitation wavelength of 325 nm and a grating with 300 l/mm. The optical properties of the samples were measured at room temperature by measuring the absorbance of the sample in the range of 200 – 800 nm. Spectrophotometry (Hitachi UV-3600) with integrating sphere attachment allowed measuring absorbance spectra for solids. Photocurrent measurements were performed into an H-cell filled with distilled water mixed with a 0.1 M of Na_2SO_4. A photoanode made of the GNS/TiO_2 nanocomposites film and Pt electrodes were installed in the photoelectrochemical cell. A UV-visible lamp with a spectral range (315–450 nm) (UV 400 HL230 Fe Clear-A, UV Light Technology Limited, Birmingham, UK) with a power density of 100 mW/cm^2 was used.

Photocatalytic degradation processes

Photocatalytic degradation of the colored pollutants was studied through determining the photocatalytic activity of the prepared samples. The used photochemical reactor was the source for the quartz immersion well reactor (RQ400), which was used for performing photocatalytic reactions. The double-walls of the immersion well were used for cooling the lamp during the photocatalytic reactions. The mercury lamp, which has 400 W medium pressure, was combined with 400 mL standard reaction flask to carry out the photocatalytic reactions. A major part of radiation for medium pressure lamp focuses in the range of 365-366 nm. In the current study, photocatalytic reactions were performed with the Naphthol Green B dye. A low 4×10^{-4} M concentration aqueous solution of the dye was prepared. The amount of photocatalyst was 0.3 g/L. By measuring the maximum of the band in the spectrum of the dye, the concentration of the dye can be determined by the Beer–Lambert law. The characteristic band of the Naphthol Green B is at 714 nm. Therefore, the concentration change of the dye was monitored by measuring the absorbance at 714 nm. The experiment was performed in the dark for 60 mins to avoid the adsorption process between the photocatalyst and the dyes. Also, this experiment was carried out without photocatalyst in presence of UV light for 60 mins to test the stability of the dye. After irradiation with UV light, small doses of the solution were withdrawn at different intervals of time. By UV-Vis absorption, the concentration of the remaining dye in the solution was determined.

Results and discussion

XRD

X-ray diffraction measurements were performed onto 4 samples: pure TiO_2 with a size of 20 nm, GNS/TiO_2 (20 nm), pure TiO_2 with a size of 5 nm, and GNS/TiO_2 (5 nm). Figure 1a shows XRD patterns of anatase phase of TiO_2 with its diffraction peaks located at 25.3, 37.9, 48.05, 53.9, 55.06, 62.4, 68.76, 70.3 and 75.06 assigned to the respective crystalline planes (101), (004), (200), (105), (211), (204), (116), (220) and (215), as reported in JCPDS card no. 21-1272. However, no pattern related to gold was observed because the gold concentration was too low. If we compare pure 5 nm TiO_2 and 20 nm TiO_2, the size effect is clearly observed through the broadness and the shift of the (101) crystal plane peak, decreasing with the size going from 20 down to 5 nm, see Figure 1b. To confirm the origin of the shift, the lattice parameters, namely the interplanar distance d and the crystallite size D, were extracted from the XRD patterns, see Table S1. The crystallite size D was extracted using Debye-Scherrer equation for the two crystal planes (101) and (200) [52]. As expected, the crystallite size in the 5 nm TiO_2 nanoparticles is half that of the 20 nm TiO_2 ones. The interplanar distance d is larger in the case of the 5 nm TiO_2, d = 3.548 Å, as compared to the 20 nm TiO_2, d = 3.521 Å. These values are comparable to that found in studies focusing on Au@TiO_2 core shell and Au/TiO_2

nanocomposites [46,53–57]. The latter is due to the increasing strain when the size decreases [58]. However, the shift between the GNS/TiO_2 5 nm and the 20 nm samples at large diffraction angles is due to the presence of the gold nanoparticles. The physical origin of this shift is due to a compressive effect on the lattice parameters at the nanoparticles surface [59]. This shift is more pronounced in the 5 nm TiO_2 nanocomposites as compared to the 20 nm TiO_2, see Table S1. Indeed, the effect of the GNS on the surface structural properties in very small nanoparticles such as 5 nm GNS/TiO_2 is expected to be due to its higher surface to volume ratio at smaller sizes, see Figures S5-7.

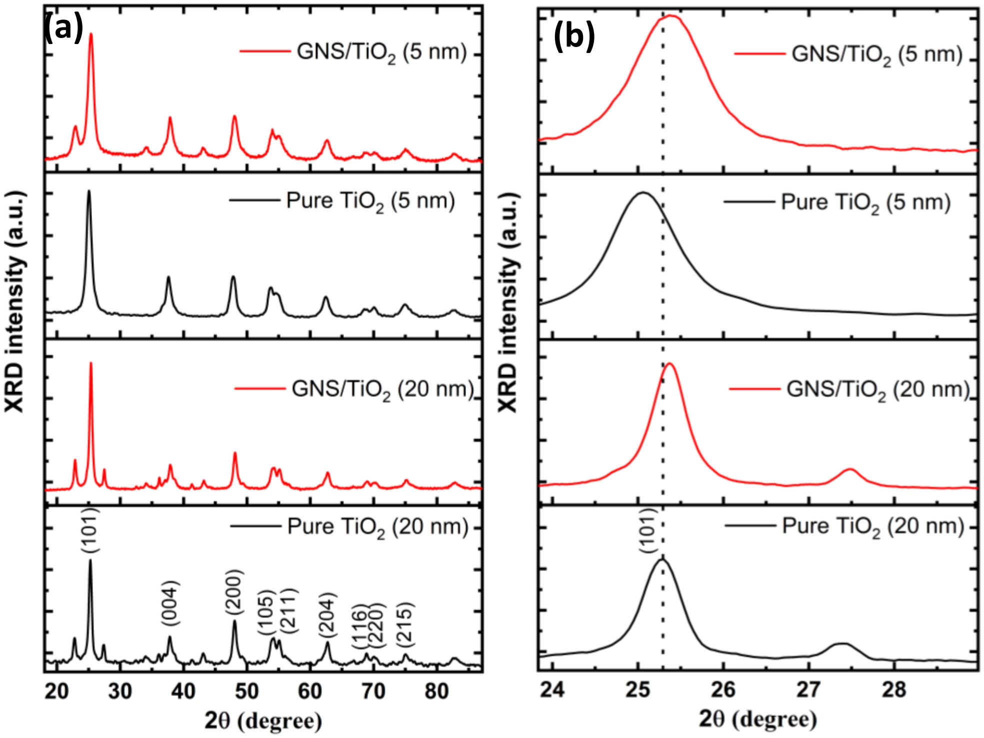

Figure 1: (a) XRD patterns of Pure TiO_2 (20 nm), GNS/TiO_2 (20 nm), Pure TiO_2 (5 nm), GNS/TiO_2 (5 nm). (b) Inset shows the XRD peak of (101) crystal plane where a shift is represented by a dotted line. Lattice parameters, crystallite size, and interplanar distance of TiO_2/GNS nanocomposites extracted from the XRD patterns are presented in Table S1.

TEM and EDX analysis

Figures 2 (a-b) show TEM images of GNS. It is clearly seen that GNS have an average size of 50 nm and tips with an average diameter of 10 nm. Figures 2(c-d) show TEM micrographs for the 20 nm GNS/TiO_2 sample. It can be clearly seen from the figures that the TiO_2 nanoparticles with an average size of 20 nm in addition to few gold nanostars (GNS) with an average size of 50 nm were distributed throughout the surface. Furthermore, high magnification images as shown in Figure 2 (c) show stars like morphology of gold nanoparticles thereby revealing their shape. To study the crystal structure of the prepared samples, HRTEM images revealed an interplanar distance of 0.2±0.02 nm which corresponds to the (111) plane of gold crystal, see Figure S2 (A, B). This d spacing matches well with what has been reported in previous studies [53,60–62]. SAED patterns show clearly the rings that correspond to the (111), (200), (220), (311) and (222) planes of gold, see Figure S4 (C). To study the elemental characteristics of the nanocomposites, elemental mapping and energy dispersive spectra were performed see Figures 2(e, f) and S4(D-G). The weight percentage are 20±0.1, 72±0.5, and 7±0.2 % for O, Ti, and Au, respectively. The atomic percentage are 44±0.1, 54±0.15, and 1.3±0.02% for O, Ti, and Au, respectively.

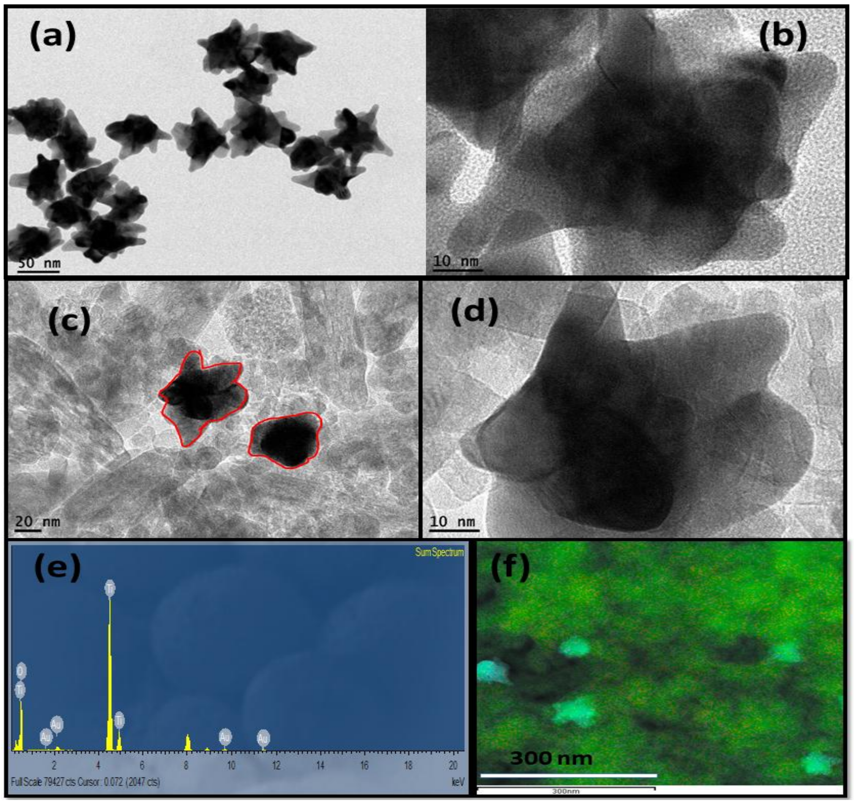

Figure 2: (a-b) TEM images of gold nanostars. (c-d) TEM image of 20 nm GNS/TiO_2 nanocomposites. (e) EDX analysis of 20 nm GNS/TiO_2 nanocomposites. The weight percentages are 20±0.1, 72±0.5, and 7±0.2 % for O, Ti, and Au, respectively. The atomic percentage are 44±0.1, 54±0.15, and 1.3±0.02% for O, Ti,

and Au, respectively. (f) Elemental mapping of Ti, O and Au represented by green, red, and blue colors, respectively.

The presence of Ti, O, and Au is clearly seen, confirming the formation of GNS/TiO_2 nanocomposites. HRTEM images also confirmed in the 5 nm GNS/TiO_2 sample the presence of TiO_2 nanoparticles with an average size of 5 nm and few gold nanostars (GNS) distributed with an average size of 50 nm, as shown in Figure 3(a)-(b). In these figures, the GNS are covered with the 5 nm TiO_2 nanoparticles and therefore the GNS tips are not well displayed. HRTEM shows different crystal plane orientations for gold and TiO_2 nanoparticles. A 0.33 nm interplane distance for the (101) plane in TiO_2 was estimated and shown in Figure S5(A, B). The approximately same distance was reported in previous works [27,60–62]. SAED patterns show clearly the rings corresponding to the (101), (004), (200), (211) and (204) planes, see Figure S3(C). Figures 3(c-d) and S5(D-G) show the energy dispersive spectra and elemental mapping of the 5 nm GNS/TiO_2 nanocomposites. The presence of Ti, O, and Au in the 5 nm GNS/TiO_2 nanocomposites are clearly seen. The weight percentages are 29±0.15, 56±0.4, and 15±0.2 % for O, Ti, and Au, respectively. The atomic percentages are 59±0.3, 38±0.4, and 2.5±0.03% for O, Ti, and Au, respectively.

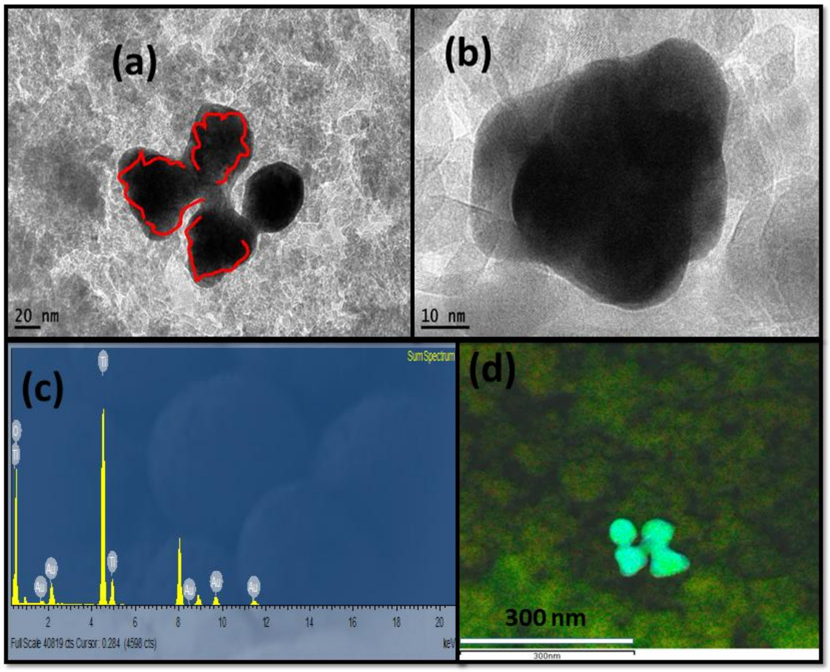

Figure 3: (a-b) TEM images of 5 nm GNS/TiO_2 nanocomposites (c) EDX analysis of 5 nm GNS/TiO_2 nanocomposites. The weight percentages are 29±0.15, 56±0.4, and 15±0.2 % for O, Ti, and Au, respectively. The atomic percentages are 59±0.3, 38±0.4, and 2.5±0.03% for O, Ti, and Au, respectively. (f) Elemental mapping of Ti, O and Au represented by green, red, and blue colors, respectively.

Raman spectroscopy

Figure 4(a) shows the Raman spectra of 20 nm GNS/TiO_2 nanocomposites and 20 nm pure TiO_2. In the two spectra, phonon modes located at 143 cm^{-1}, 195 cm^{-1}, 396 cm^{-1}, 515 cm^{-1} and 635 cm^{-1} were observed. These observed phonon modes purely belong to the anatase phase. The space group for tetragonal anatase is $I_{4_1/amd}$ and the point symmetry is D_{2d}. The two TiO_2 units present in the primitive cell give six Raman–active fundamental modes in the phonon spectrum, namely three E_g, two B_{1g} and one A_{1g} modes [49]. The inset in Figure 4(a) shows a blue shift of 0.8±0.03 cm^{-1} with a width of 1.1±0.04 cm^{-1} for the E_g mode resulting from the GNS effect incorporated into the TiO_2 nanoparticles [63,64]. This shift and width induced by the presence of the gold nanoparticles were also reported in different studies [46,61,62,65]. Figure 4(b) shows the Raman spectra of 5 nm GNS/TiO_2 nanocomposites and 5 nm pure TiO_2. We observe in the two spectra the phonon modes located at 147 cm^{-1}, 195 cm^{-1}, 395 cm^{-1}, 514 cm^{-1} and 638 cm^{-1}. A blue shift of 1.2±0.02 cm^{-1} and a width of 1.9±0.04 cm^{-1} are observed for the $E_g$mode resulting from the GNS effect on TiO_2, see Table S2. From this analysis, it is concluded that the 5 nm TiO2 nanoparticles are more affected by the GNS presence than the 20 nm due to their smaller size and thus larger surface to volume ratio and its LSPR located closer to the exciting laser wavelength than the 20 nm TiO2 nanoparticles. The blue shift observed for the pure 5 nm TiO_2 as compared to the 20 nm TiO2 nanoparticles is therefore due to the size dependent confinement effect [66].

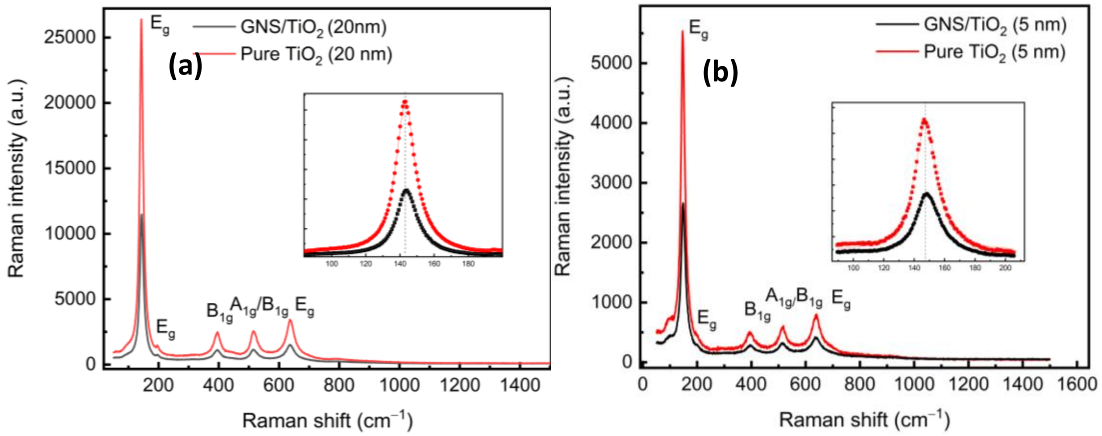

Figure 4: (a) Raman spectra of pure TiO2 (20 nm) and GNS/TiO2 (20 nm) nanocomposites. Inset shows the blue shift observed in GNS/TiO2 (20 nm) regarding pure TiO2, (b) Raman spectra of pure TiO2 (5 nm) and GNS/TiO2 (5 nm) nanocomposites with corresponding inset as in (a). The peak position and FWHM extracted from E$_g$ phonon mode using a Lorentzian function are presented in Table S2.

UV-visible absorption and Tauc plot

TiO_2 is one of the most efficient photo-active materials, as reported in literature[67]. Yet, there has been many studies reporting changes in the structure, the size and the morphology of TiO_2 to decrease its band gap and improve its efficiency. Decorating TiO_2 nanoparticles with plasmonic nanoparticles is one promising approach for improving the optical properties. In this respect, the optical behavior of the GNS/TiO_2 nanocomposites was also studied by UV-Visible absorption spectroscopy to provide further details about absorbance and band gaps.

Figure 5(a) shows that the 5 nm TiO_2 nanoparticles absorb actively in the UV region with a broad absorption band in the [200–350 nm] wavelength range. This broad absorption band may be due to the typical electronic transition from the O 2p to the TiO_2 3d orbital. Upon incorporation of GNS into the 5 nm TiO_2 nanoparticles, a new band is observed in the visible region at 600 nm as shown in Figure 5(b). This band is attributed to the GNS LSPR. This result agrees well with the reported data by Wan et al. [68]. They indicated that the enhanced absorption range from 400 to 800 nm with a broad absorption peak at about 600 nm results from the LSPR of the Au nanoparticles. It is indeed reasonable since the Au nanoparticles LSPR is sensitive to the size and the surrounding environment. To extract the band gap energy of the pure and the GNS nanocomposites TiO_2

nanoparticles, we plotted the data using Tauc equation. The wide band gap is estimated at room temperature to be 3.4±0.04 eV in accordance with the electronic transition from the valence band to the conduction band of anatase TiO_2 as seen in Figure 5(c). A slight narrowing of the band gap energy for the 5 nm TiO_2 nanoparticles was though observed in presence of the gold nanoparticles as seen in Figure 5 (d). The band gap energy of the 5 nm GNS/TiO_2 nanocomposites decreased to 3.2±0.03 eV.

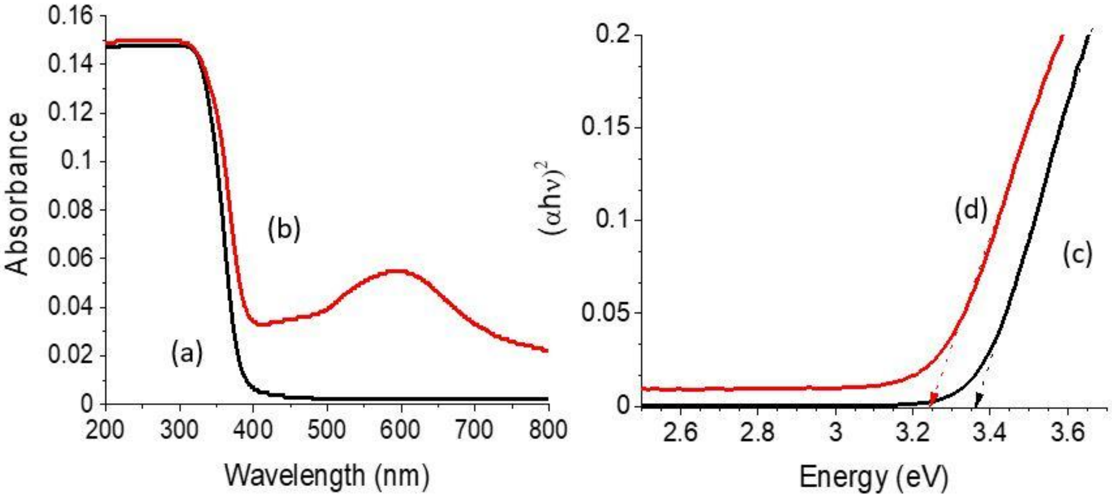

Figure 5: UV-Vis absorbance of (a) PureTiO_2 (5 nm) nanoparticles, (b) GNS/TiO_2 (5 nm) nanocomposites and indirect band gap energy measurement using Tauc plot: (c) PureTiO_2 (5 nm) nanoparticles, (d) GNS/TiO_2 (5 nm) nanocomposites.

This behavior was compared to that of the 20 nm TiO_2 nanoparticles, see Figures 6(a)-(d). The 20 nm TiO_2 nanoparticles have a wider band gap, the edge of the absorbance being shifted to 400 nm. This effect was confirmed through calculating its band gap energy. Figure 6(c) shows that the band gap energy decreased from 3.4±0.04 eV to 3.2±0.01 eV. In addition, incorporating the GNS improved the optical properties of the nanocomposite with the appearance of a new absorption band in the visible region at 680 nm as shown in Figure 6(b). This feature was accompanied by the narrowing of the band gap found to be 3.1±0.03 eV, as seen in Figure 6(d). It is therefore clearly seen that the effect of the smaller size is to introduce the blue shift of the GNS LSPR band for the 5 nm GNS/TiO_2 composite positioned around 600 nm as compared to that of the 20 nm GNS/TiO_2 composite positioned around 680 nm, a shift of about 0.2 eV. Such a large wavelength shift results from the large sensitivity of the GNS morphology to the environment changes as compared to the spherical morphology [69]. We therefore conclude that a strong synergetic effect is observed between the GNS and the TiO_2 nanoparticles with size 5 nm as compared to size 20 nm.

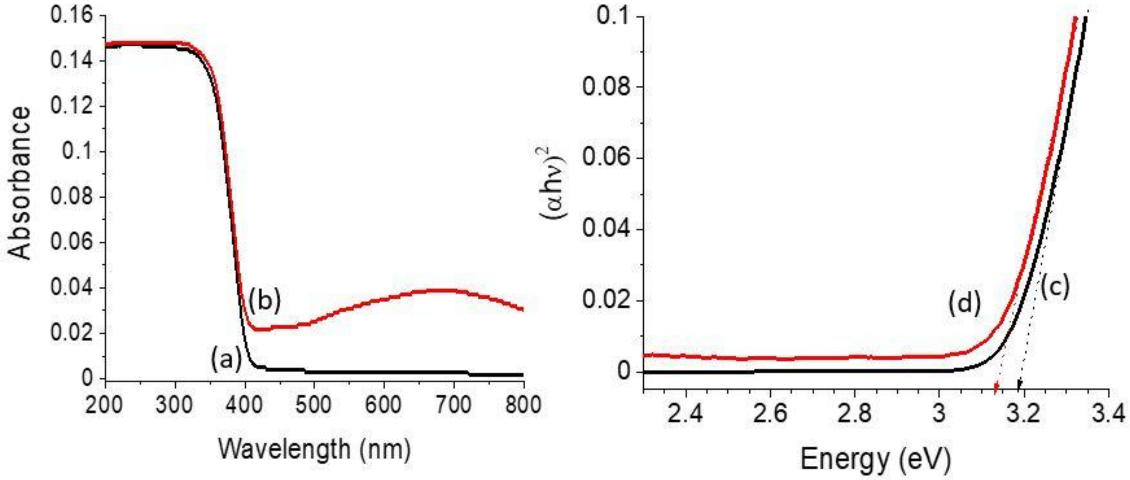

Figure 6: UV-Vis absorbance of (a) TiO_2 (20 nm) nanoparticles (b) GNS/TiO_2 (20 nm) nanocomposites and indirect band gap energy measurement using Tauc plot of: (c) TiO_2 (20 nm) nanoparticles, (d) GNS/TiO_2 (20 nm) nanocomposites.

Photocurrent Study

Figure 7 shows the variation of the photocurrent as a function of time for different films of pure 5 nm TiO_2, GNS/5 nm TiO_2, pure 20 nm TiO_2 and GNS/20 nm TiO_2 with an applied bias voltage of 0.5 V. The presence of the GNS increased significantly the photocurrent with respect to the corresponding pure TiO_2. Globally, the 5 nm TiO_2 nanoparticles showed more photocurrent than the 20 nm ones due to their smaller size. The results confirmed that the presence of gold nanoparticles slowed down the electron-hole recombination rate and hence increased the photocurrent. The higher surface to volume ratio at smaller size thus increased the photoelectrochemical water splitting on the photoanode. The latter proved that the lifetime of the photoelectron hole recombination is longer in the case of the 5 nm TiO2 nanocomposites. The photocurrent densities measured by irradiating the different films, namely 5 nm TiO_2, GNS/5 nm TiO_2, pure 20 nm TiO_2 and GNS/20 nm TiO_2 using UV-visible light were 2, 3.5, 1.5 and 1 μA/cm^2 respectively. These values are consistent with those obtained by H. Wang et al. and H. Chen et al. [60,61,70].

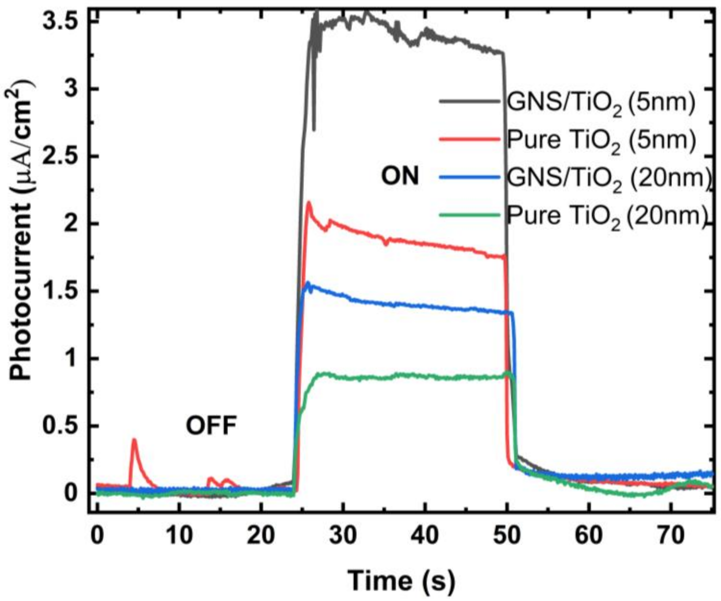

Figure 7: photocurrent versus time for different films of 5 nm TiO_2, GNS/5 nm TiO_2, pure 20 nm TiO_2 and GNS/20 nm TiO_2. A bias voltage of 0.5 V was applied during a light irradiation.

Photoluminescence Study

PL measurements showed the presence of different bands located at 420, 522, and 588 nm. The excitation laser wavelength used here was 325 nm that is above the bang gap energy of all the samples, see Figure 8. Therefore, the observed emissions are due to the radiative recombination of free electrons in conduction band with holes in defect states and valence band. Let's discuss the peak located at 422 nm, this emission is close to the band gap edge of nanocomposites and reflects more the effect of gold nanoparticles on the separation and migration of excitons in the nanocomposites. It is clearly seen that PL intensity increases in this order GNS/TiO_2 (5 nm), TiO_2 (5 nm), GNS/TiO_2 (20 nm), and TiO_2 (20 nm). The results confirmed how GNS slow down the recombination rate of e^- – h^+ pairs by capturing electrons. It was reported UV light induced, the photogenerated electron in conduction band of TiO_2 to migrate to gold, when the two-fermi level are matched, this is called interfacial charge transfer. TiO_2 (20 nm) showed a faster recombination rate than TiO_2 (5 nm), this could be explained by the non-radiative emission induced by the more state occupied by surface trapped electron state in very small nanoparticles with 5 nm average size. This non-radiative emission is confirmed by the increase in the radiative emission of 522 and 588 nm that is due to the deep trap excitons. It is localized above the fermi level or below it under equilibrium before laser excitation. These electrons can promote transition to trapped h^+ in valence band or near the states above it. These results correlate well with the photocurrent study

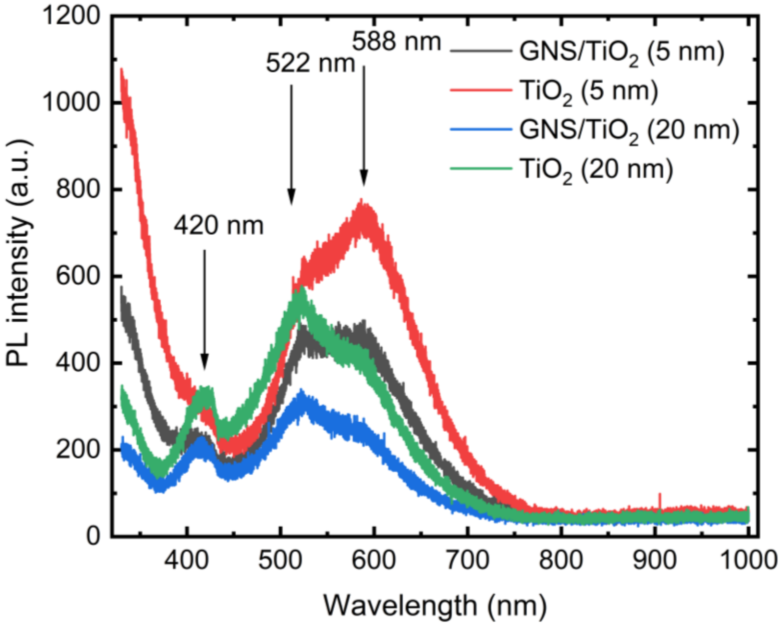

Figure 8: PL intensity as function of wavelength performed, at an excitation laser wavelength of 325 nm, for pure TiO_2 (5 nm), GNS/TiO_2 (5 nm), pure TiO_2 (20 nm), and GNS/TiO_2 (20 nm).

Photocatalytic study

In the present study, the photocatalytic activities and performance of the GNS/TiO_2 nanocomposites were also studied and compared to the pure TiO_2 nanoparticles for the photocatalytic degradation of the Naphthol Green B dye used as an example for industrial pollutants [67,71]. The photocatalytic experiment was carried out by sending UV light (400 W, medium pressure mercury lamp) to the aqueous solution containing the dye in presence of the photocatalysts. The Naphthol Green B concentration was monitored by measuring the UV-visible absorbance of the liquid solution as a function of time. The decay of the Naphthol Green B concentration was then determined with the decrease of the absorbance at its maximum located at λ_{max} = 714 nm as seen in Figures 9.

The blank experiment performed without any catalyst indicated that the Naphthol Green B dye is a rather stable molecule against UV-light. This feature shows that photolysis can be ruled out as a mechanism for dye degradation. When the sample solution was stirred for 60 mins in the dark, no change was detected in the dye concentration.

Figure 9(a,b) shows the photocatalytic degradation of Naphthol Green B under UV light with the 20 nm TiO_2 composite, as seen from the decrease of the maximum absorption at 714 nm. After 70 mins of UV irradiation time, the disappearance of the solution color was observed confirming the full degradation for the dye. With the 5 nm GNS/TiO_2 composite, the Naphthol Green B totally disappeared in a time shorter than that observed for the 20 nm TiO_2. Figure 9(c,d) further reveals that the photocatalytic degradation process of Naphthol Green B is achieved in 15 mins only with the 5 nm GNS/TiO_2 composite as compared to the 70 mins with the 20 nm TiO_2 composite. The photocatalytic process is thus much faster in the presence of the GNS and smaller TiO_2 nanoparticles, a feature attributed to the GNS LSPR induced band gap shift. This behavior is also found with the 5 nm TiO_2 nanoparticles and the 5 nm GNS/TiO2 nanocomposite samples. With and without the presence of the GNS, these samples are more efficient than the two previous 20 nm TiO_2 and 20 nm GNS/TiO_2 samples, indicative of an improved efficiency of the smaller size towards the photocatalytic degradation of Naphthol Green B, see Figures 9(a, b). The latter is confirmed by the large specific area of the 5 nm GNS/TiO_2, namely $a_{s,BET}$=141 m^2/g as compared to that of the 20 nm GNS/TiO_2, $a_{s,BET}$=75 m^2/g, see Figure S4-6. Consequently, the Naphthol Green B absorbance maximum at 714 nm disappears after 19 mins only of UV light irradiation as seen in Figure 9(a, b). Compared with the 20 nm GNS/TiO_2 nanocomposite sample, acceleration of the degradation of Naphthol Green B is observed with a total degradation of Naphthol Green B performed in 10 mins only, see Figure 9(c, d).

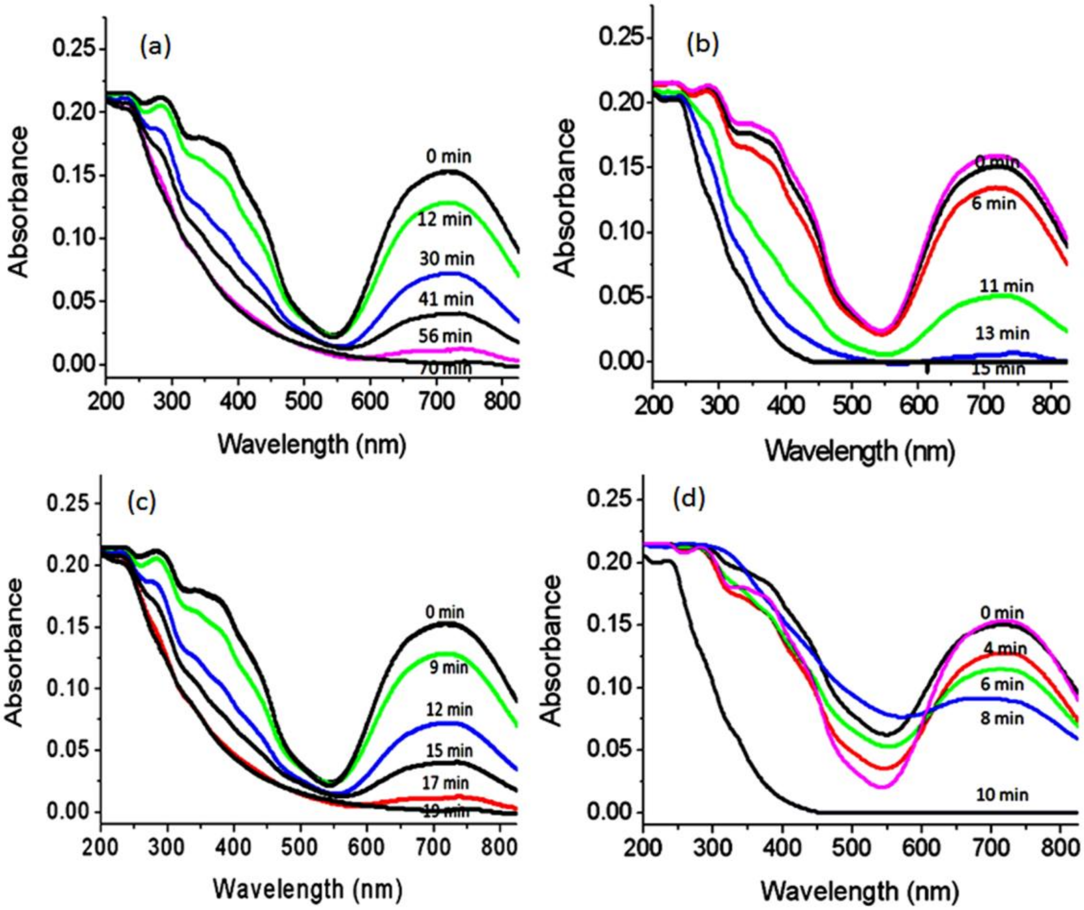

Figure 9: Photocatalytic degradation of Naphthol Green B in presence of: (a) 20 nm TiO_2 nanoparticles, and (b) GNS/20 nm TiO_2 nanocomposites. (c) 5 nm TiO_2 nanoparticles and (d) GNS/5 nm TiO_2 nanocomposites. Absorbance versus wavelength was measured for different irradiation time.

The high performance and activity of the nanocomposites, either the 5 nm GNS/TiO_2 or the 20 nm GNS/TiO_2 nanocomposites, as compared to the pure TiO2 counterparts is explained according to the presence of the LSPR in GNS. The gold nanoparticles dispersed in the semiconductor underwent interfacial charge transfer with the titanium oxide. Under UV light, the electrons of titanium oxide were excited from the valence band to the conduction band. These electrons in the conduction band of titanium oxide migrated to the surface of the gold nanoparticles because gold has a lower Fermi-level energy. The Schottky barrier produced at the interface between titanium oxide and gold trapped the electrons and thereby slowed down the recombination rate of the charge carriers causing the higher performance for the degradation of the organic dye.

Quantification of the higher performance of the 5 nm and 20 nm GNS/TiO_2 nanocomposites can thus be obtained with a kinetic study of the dye degradation using the following rate equation:

$$\ln [C_o/C(t)] = k \times t \qquad (1)$$

with the constant rate of reaction k, the initial concentration C_0 of Naphthol Green B dye and the concentration of Naphthol Green B at different times C(t). According to Figure 10 where $\ln(C_o/C)$ is plotted against the illumination duration in minutes, it is confirmed that the photocatalytic degradation and decolorization of the Naphthol Green B dye solution process is a pseudo-first order reaction for both the pure TiO_2 and GNS/TiO_2 nanocomposite systems.

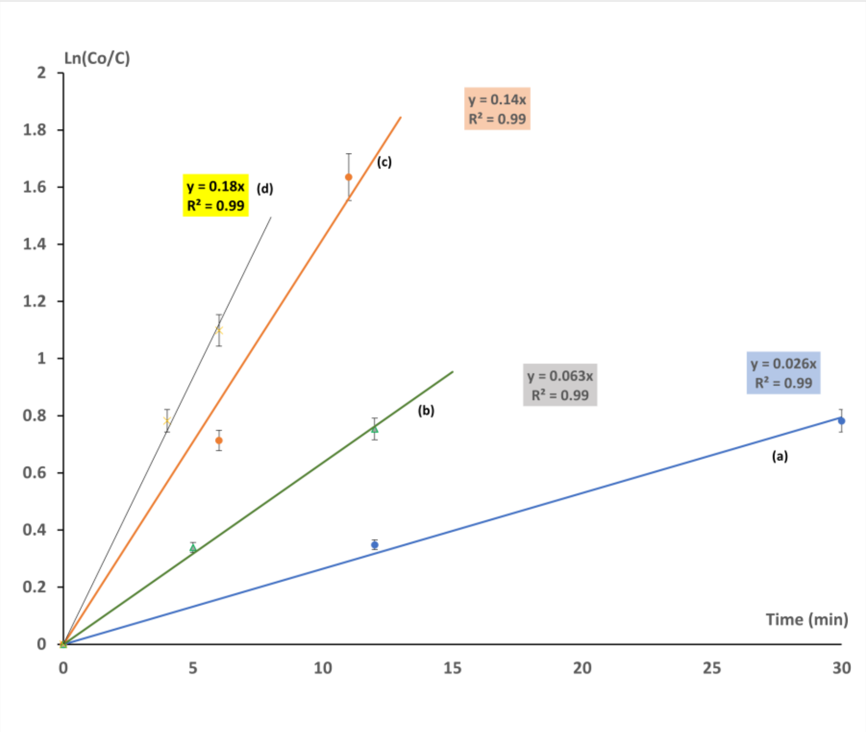

Figure 10: Kinetics process of the Photocatalytic deterioration of Naphthol green B in presence of: (a) 20 nm TiO_2, (b) 5 nm TiO_2, (c) GNS/TiO_2 (20 nm) nanocomposites and (d) 5 nm GNS/TiO_2 (5 nm) nanocomposites. The data was adjusted with a linear function. R-squared is 0.99 for all the samples.

From Figure 10, the reaction rate constant k for the Naphthol Green B dye degradation with the 20 nm TiO2 sample is 0.026±0.005 min^{-1}. With the change of the TiO_2 particle size from 20 nm down to 5 nm, the reaction becomes faster and the reaction rate constant is found to be 0.063±0.006 min^{-1}. However, even faster reactions are observed for the GNS/TiO_2 nanocomposite samples, 0.14±0.01 min^{-1} and 0.18±0.02 min^{-1} for 20 nm GNS/TiO_2 and 5 nm GNS/TiO_2 respectively. This kinetics study concludes that k can become as large as twice for the GNS/TiO_2 nanocomposite samples as compared to the pure TiO_2 nanocomposite ones.

Mechanism of the photocatalytic process

The reaction mechanism of the photocatalysis depends on the separation process between electrons and holes when exposed to UV light as seen in Eq. (1). With UV light irradiation, the electrons are excited from the valence band to the conduction band leaving holes in the valence band. Accordingly, oxygen molecules react with the excited electrons to become strong oxidizing agents $^{\bullet}O_2^-$ as seen in Eq. (2). Meanwhile, water molecules react with the valence band holes to produce the highly oxidizing $^{\bullet}OH$ radicals as shown in the following equations:

$$\text{Au-Ti} + \text{light} \rightarrow h^+ \ (\text{Valence band}) + e^- \ (\text{Conduction band}) \qquad (1)$$

$$O_2 + e^- \rightarrow {}^{\bullet}O_2^- \qquad (2)$$

$$H_2O + h^+ \rightarrow \bullet OH + H^+ \qquad (3)$$

$$\text{NG dyes} + \text{oxidizing agents} \rightarrow CO_2 + H_2O \qquad (4)$$

In addition, the oxidizing agent (•O2$^-$) can react with H+, produced in Eq.(3) to increase the concentration of •OH radicals through the series of reactions as follow:

$$H+ \ + \bullet O_2^- \rightarrow \bullet HO_2 \qquad (5)$$

$$2 \bullet HO_2 \rightarrow H_2O_2 + O_2 \qquad (6)$$

$$H_2O_2 + e^- \rightarrow \bullet OH + OH^- \qquad (7)$$

$$\text{NG dyes} + \text{oxidizing agents} \ (\bullet OH) \rightarrow CO_2 + H_2O \qquad (8)$$

In the current study, the high photocatalytic activity of the pure 5 nm TiO_2 and 5 nm GNS/TiO_2 nanocomposites can be explained by the smaller size of the TiO_2 nanoparticles creating photo-active centers. This feature leads to an increase of photocatalytic activity through the production of a large amount of strongly oxidizing agents as shown in Eqs. (2) and (3). These oxidizing agents lead to the full degradation of organic dye as shown in Eq. (4, 8).

In addition, for the 5 nm GNS/TiO_2 nanocomposite, a new feature occurs with the presence of the GNS LSPR. The gold nanoparticles dispersed in the semiconductor undergo interfacial charge transfer with TiO_2. BET study showed that GNS/TiO_2 (5 nm) has a specific surface area of $a_{S,BET}$=141.06 m^2/g and $a_{S,\ BET}$=75.261 m^2/g for GNS/TiO_2 (20 nm), see Figure S7. These results promote a strong adsorption and interaction between the surface of TiO2 and GNS for the case of 5 nm size compared to the 20 nm. In fact, GNS shape implies tips where local field enhancement is rather large than other shapes. As a result, this shape is much more sensitive to environmental changes that could result when very small TiO_2 nanoparticles are in contact with GNS. This funding was confirmed by the more pronounced shift observed in XRD and Raman. The excited electrons in the TiO_2 conduction band migrate to the surface of the gold nanoparticles because gold has lower Fermi-level energy. Thus, the Schottky barrier produced at the interface of TiO_2 and gold can trap the electrons. This barrier leads to an accelerating charge separation process between the electrons and holes in addition to preventing their recombination reaction therefore causing a high efficiency for organic dye degradation. PL and photocurrent studies proved that GNS/TiO_2 (5 nm) exhibited a very slow recombination rate of $e^- h^+$ pairs compared to other nanocomposites. To compare and evaluate our results to other studies, Table 1 showed some reported studies with nanocomposites similar to our samples. It is clearly seen that the kinetic reaction rate measured for the GNS/TiO_2 nanocomposites is much higher than those reported for other systems, as mentioned in Table 1. In most studies, the size of nanocomposites is larger than our sizes and their dyes are less heavy and complex. This confirm the importance of using the very small size of TiO_2 that showed strong synergetic effect although the quantity of GNS is very low.

Table 1: Comparison between pseudo first order kinetic reaction rate k in this work as compared to those reported in other works with similar nanocomposites with different average size, dye, and fabrication method.

References	**Samples**	**Average size (nm)**	**Dye**	**Pseudo first order kinetic reaction rate /min^{-1}**
This work	Gold/TiO_2 nanocomposites	5-20	Naphthol Green B	0.18
F. Azeez et al. [72]	Pure TiO_2	10	Methylene blue	0.018
X. Yang et al. [63]	Au and Ag decorated TiO_2	3.5	Methylene blue	0.032
Lidiaine M. Santos et al. [73]	Ag-TiO2	10-27	E102 tartrazine dye	0.076
Sadaf Bashir Khan et al. [74]	Zig-Zag TiO_2	20	Methyl orange	0.019
Al Suliman et al[75]	Ag-TiO_2	200-500	Methylene blue	0.050
L. P. Wu et al.[61]	Au/TiO_2 nanotubes	10-30	Tetracycline	0.020
L. Wu et al. [62]	Au@TiO_2 core -shell	500	Methyl orange	0.069

To correlate between the kinetic reaction rate values and bad gap, we summarized the calculated values in a comparison table, see Table 2. After adding GNS to TiO_2, the kinetic reaction rate k increased for 5 nm GNS/TiO_2 and 20 nm GNS/TiO_2. This increase was more pronounced for the 20 nm TiO_2 than for the 5 nm TiO_2. But although the observed increase, GNS/TiO_2 (5 nm) is still higher than others, see Table 2. When looking carefully at the band gap values, these values are close each to other, this confirm that the band gap values less impact than other factors such as the size, surface area, crystallinity, etc. This work opens the way to further study the system again by tuning and expanding the excitation wavelength during the photocurrent studies and GNS concentration.

Table 2: Comparison between the band gap energy and pseudo first order kinetic reaction rate of GNS/TiO_2, and the ratio between k of pure TiO_2 (5 nm) and GNS/TiO_2 (5 nm) and between pure TiO_2 (20 nm) and GNS/TiO_2 (20 nm).

Sample	Band gap energy (eV)	Pseudo first order kinetic reaction rate /min^{-1}
Pure TiO_2 (5 nm)	3.4±0.04	0.063±0.006
GNS/TiO_2 (5 nm)	3.2±0.01	0.18±0.02
Pure TiO_2 (20 nm)	3.2±0.03	0.026±0.005
GNS/TiO_2 (20 nm)	3.1±0.03	0.14±0.01

Computational Modeling

To examine further the effect of GNS on TiO_2, a computational study was performed with the Quantum Atomistix ToolKit (quantumATK)[76] package [74], employing the method of local combination of atomic orbitals (LCAO). The exchange–correlation potential was described by the GGA-PBE functional[77]. To calculate the self-consistent field (SCF), a threshold limit of 10^{-6} eV for energy convergence was used. The geometrical framework and atom relaxation were relaxed to a force on each atom of less than 0.05 eV/Å using the Broyden—Fletcher—Goldfarb—Shanno (LBFGS) approach. The optimized lattice parameters were found to be $a = b = 3.7746$ Å, $c = 9.6280$ Å, in good agreement with the experimental values of $a = b = 3.7848$ Å, $c = 9.5124$ Å[78]. At the same time, the calculated lattice constant of Au with face-centered cubic structure is 4.113 Å. In this study, we deal with a simple interface slab model of Au (001)/anatase TiO_2 (001). Figure 11(a) shows a unit cell of the model system consisting of two Au layers epitaxially built on a TiO_2 layer immersed in vacuum[79]. For investigating the stability of the Au/TiO_2 composite interface system, the formation energy of the interface was computed by the following formula: $E_f = (E_{Au/TiO2} - E_{Au} - E_{TiO2})/S$ where E_{Au}, E_{TiO2} and $E_{Au/TiO2}$ represent the total energies of the Au slab, the TiO_2 slab and the composite system, respectively with S the area of the interface. The distance between the Au and TiO_2 planes at the interface is found to be 2.3 Å. It is found that the E_f of -0.130 eV/$Å^2$ has a negative value indicating that the Au/TiO_2 composite interface system is stable. This result is in good agreement with other theoretical studies[79]. To investigate the electronic properties of this Au/TiO_2 composite interface system, the layered decomposed densities of states (DOS) were calculated and are displayed in Figure 12(a). It is observed that the LDOS of the TiO_2 substrate layer is very similar to the DOS of bulk anatase[46,78–80]. In the LDOS of the interfacial TiO_2 layer, it can be observed that the induced gap states are represented as a continuous spectrum of states in the band gap. To investigate the distribution and hybridization of the electron states at the interface, local and partial density of states of the Au/TiO_2 composite interface are depicted in Figure 12(b). The bottom of the conduction band is mostly composed of the hybridization between Ti 3d states and O 2p states while the top of the valence band mainly consists of Au 5d states. The interfacial states can be ascribed to the strong interaction between the Au layer and TiO_2 layer. To visualize the charge transfer at the Au and TiO_2 interface, the charge density difference was calculated and is presented in Figure 12(c). It is observed that the positive electronic charges (yellow color) are seen around the O atoms whereas the negative electrons (green color) are observed around the Ti atoms. Moreover, charge redistribution is found to occur between the Au and the O atoms. Therefore, the Au atoms bonded with O atoms gain some electrons. The study reveals electron migration from the TiO_2 layer to the Au layer. Additionally, this charge transfer induces a potential drop (ΔV) across the Au/TiO_2 interface, as illustrated in Figure 12(d). The potential decreases by 8.01 eV from the TiO_2 layer to the Au layer. We also carried out calculations of the plane-averaged electrostatic potential along the z-direction for the TiO_2 /Au interface, as shown in Figure 12(d). The results reveal a substantial potential difference of 8.01 eV across the interface, indicating the presence of a strong built-in electric field. This internal field arises from the significant electrostatic potential gradient at the interface and is particularly advantageous, as it can effectively promote the separation of photogenerated charge carriers, thereby enhancing the overall photocatalytic efficiency [81,82]. To study the interactions between Naphthol Green B and the Au/TiO_2 composite interface, see Figure 12(b), the adsorption energy of Naphthol Green B on the Au/TiO_2 composite was computed using the following expression[83,84] $E_{ads} = E_{\mathrm{NaphtholGreenB}-Au/TiO2} - E_{Au/TiO2} - E_{\mathrm{NaphtholGreenB}}$ where $E_{NaphtholGreenB\text{-}Au/TiO2}$, $E_{Au/TiO2}$ and $E_{\mathrm{NaphtholGreenB}}$ denote the total energy of the Naphthol Green B - Au/TiO_2

complex, the Au/TiO_2 composite interface and the isolated Naphthol Green B dye respectively. The calculated E_{ads} is found to be -4.62 eV, showing strong adsorption energy.

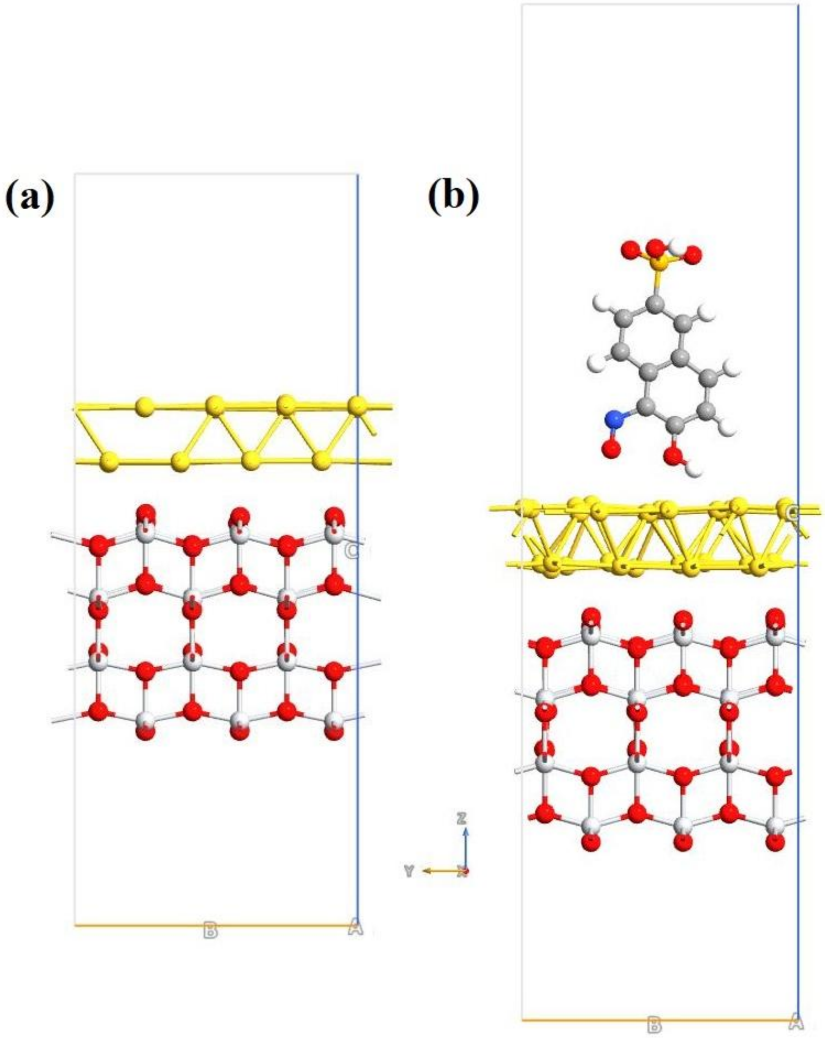

Figure 11: (a) The side view of the Au(001)/TiO_2(001) interface model and (b) the adsorption of Naphthol green B on Au/TiO_2 composite interface. Au, O, Ti, N, C, H, and S atoms are represented by yellow, red, light gray, blue, dark gray, white and orange balls, respectively.

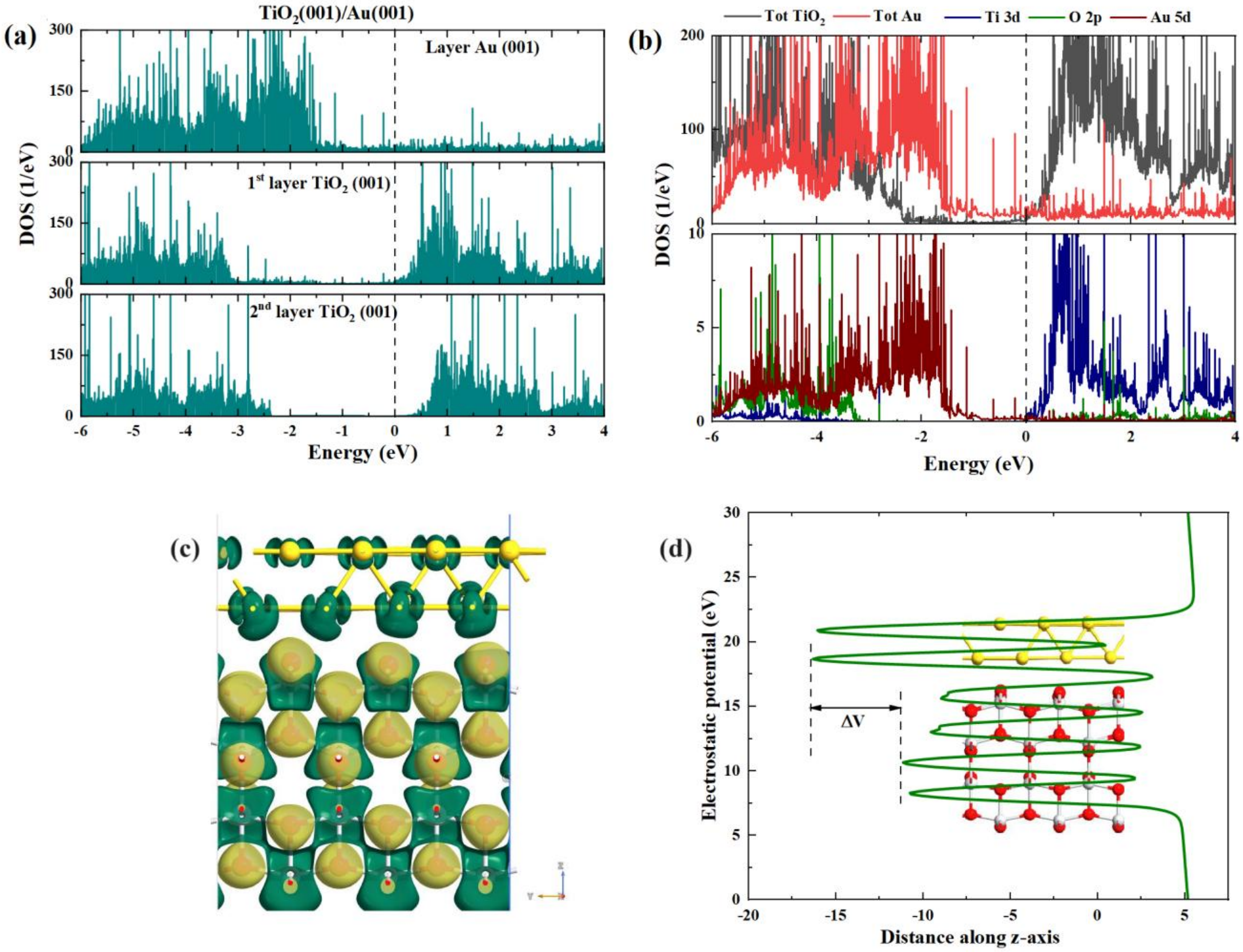

Figure 12: (a) Calculated layered decomposed DOS, (b) local and partial DOS and (c) Isosurface view of electron density difference at a value of ±0.08 electron/Å^3 for the Au/TiO$_2$ composite system, where yellow and green color denote the electron loss and gain. (d) Planar averages of the electrostatic difference potential in the Au/TiO$_2$ interface.

Conclusion

Photocurrent and photodegradation studies were conducted on GNS/TiO$_2$ nanocomposites and showed a large enhancement in the efficiency of the photo-electron conversion and ultrafast photodegradation of the Naphthol Green B organic dye due to the slow recombination rate of electrons and holes. The smaller size of the 5 nm TiO$_2$ as compared to the 20 nm TiO2 nanocomposites showed an important impact on the photocatalytic activity and the photocurrents. Kinetic reactions rates for the GNS/5 nm TiO$_2$, pure 5 nm TiO$_2$, GNS/20 nm TiO$_2$ and pure 20 nm TiO$_2$ samples were measured and found to be 0.18±0.02, 0.063±0.006, 0.14±0.01, and 0.026±0.005 min^{-1}, respectively. These observations result from the GNS LSPR induced band gap energy shifts, the electron trapping at the GNS/TiO_2 interface and the smaller size of TiO_2. With GNS, an important increase in the kinetic reaction rate of about 5 times for GNS/20 nm TiO_2, nanocomposites was observed and 3 times for the case of the GNS/5 nm TiO_2 ones. This confirms a strong synergetic effect between GNS and 20 nm TiO_2 nanoparticles in particular due to the lower band gap as compared to the pure 20 nm TiO_2 nanoparticles. Theoretical studies confirmed that the formation energy of the interface E_f is negative with a value of -0.130 eV/ $Å^2$ indicating that the Au/TiO_2 nanocomposite interface system is stable. These calculations also showed that the bottom of the conduction band is mostly arising from the hybridization between the Ti 3d states and the O 2p ones while the top of the valence band mainly consists of Au 5d states. Therefore, the Au atoms bonded with O atoms gain some electrons density. The study also reveals electron migration from the TiO_2 layer to the Au layer. Additionally, this charge transfer induces a potential drop across the Au/TiO_2 interface. This potential drop aids in the separation of the photogenerated charges. The calculated E_{ads} is found to be -4.62 eV, showing a strong adsorption energy between the Au/TiO_2 interface and the Naphthol Green B dye.

Ethical Approval

Not applicable

Conflict of Interest

There is no conflict

Availability of data and materials

The datasets used and/or analyzed during the current study available from the corresponding author on reasonable request.

Funding:

This work was supported by the Deanship of Scientific Research, Vice Presidency for Graduate Studies and Scientific Research, King Faisal University, Saudi Arabia [Grant No. KFU250195].

Supplementary data

There is supplementary data associated with this manuscript

References

[1] A. Takai, P. V Kamat, Capture, Store, and Discharge. Shuttling Photogenerated Electrons across TiO2–Silver Interface, ACS Nano 5 (2011) 7369–7376. https://doi.org/10.1021/nn202294b.

[2] S.C.Y. T. L. Phan, P. Zhang, H. D. Tran, Electron Spin Resonance Study of Mn-doped Metal Oxides Annealed at Different Temperatures, J. Korean Phys. Soc. 57 (2010) 1270–1276.

[3] M. Anpo, M. Takeuchi, The design and development of highly reactive titanium oxide photocatalysts operating under visible light irradiation, J Catal 216 (2003) 505–516. https://doi.org/https://doi.org/10.1016/S0021-9517(02)00104-5.

[4] M.K. Seery, R. George, P. Floris, S.C. Pillai, Silver doped titanium dioxide nanomaterials for enhanced visible light photocatalysis, J Photochem Photobiol A Chem 189 (2007) 258–263. https://doi.org/https://doi.org/10.1016/j.jphotochem.2007.02.010.

[5] J. Taing, M.H. Cheng, J.C. Hemminger, Photodeposition of Ag or Pt onto TiO2 Nanoparticles Decorated on Step Edges of HOPG, ACS Nano 5 (2011) 6325–6333. https://doi.org/10.1021/nn201396v.

[6] K. Awazu, M. Fujimaki, C. Rockstuhl, J. Tominaga, H. Murakami, Y. Ohki, N. Yoshida, T. Watanabe, A Plasmonic Photocatalyst Consisting of Silver Nanoparticles Embedded in Titanium Dioxide, J Am Chem Soc 130 (2008) 1676–1680. https://doi.org/10.1021/ja076503n.

[7] H.A. Atwater, A. Polman, Plasmonics for improved photovoltaic devices, Nat Mater 9 (2010) 205–213. https://doi.org/10.1038/nmat2629.

[8] M. Murdoch, G.I.N. Waterhouse, M.A. Nadeem, J.B. Metson, M.A. Keane, R.F. Howe, J. Llorca, H. Idriss, The effect of gold loading and particle size on photocatalytic hydrogen production from ethanol over Au/TiO_2 nanoparticles., Nat Chem 3 (2011) 489–492. https://doi.org/10.1038/nchem.1048.

[9] S.D. Standridge, G.C. Schatz, J.T. Hupp, Distance Dependence of Plasmon-Enhanced Photocurrent in Dye-Sensitized Solar Cells, J Am Chem Soc 131 (2009) 8407–8409. https://doi.org/10.1021/ja9022072.

[10] Y. Ide, M. Matsuoka, M. Ogawa, Efficient Visible-Light-Induced Photocatalytic Activity on Gold-Nanoparticle-Supported Layered Titanate, J Am Chem Soc 132 (2010) 16762–16764. https://doi.org/10.1021/ja1083514.

[11] G.R. Bamwenda, S. Tsubota, T. Nakamura, M. Haruta, Photoassisted hydrogen production from a water-ethanol solution: a comparison of activities of Au⍰TiO2 and Pt⍰TiO2, J Photochem Photobiol A Chem 89 (1995) 177–189. https://doi.org/https://doi.org/10.1016/1010-6030(95)04039-I.

[12] S. Sakthivel, M. V Shankar, M. Palanichamy, B. Arabindoo, D.W. Bahnemann, V. Murugesan, Enhancement of photocatalytic activity by metal deposition: characterisation and photonic efficiency of Pt, Au and Pd deposited on TiO2 catalyst,

Water Res 38 (2004) 3001–3008. https://doi.org/https://doi.org/10.1016/j.watres.2004.04.046.

[13] C. Byrne, G. Subramanian, S.C. Pillai, Recent advances in photocatalysis for environmental applications, J Environ Chem Eng (2018). https://doi.org/10.1016/j.jece.2017.07.080.

[14] M. Jakob, H. Levanon, P. V Kamat, Charge Distribution between UV-Irradiated TiO2 and Gold Nanoparticles: Determination of Shift in the Fermi Level, Nano Lett 3 (2003) 353–358.

[15] S. Bahrami, A. Ahmadpour, T. Rohani Bastami, A. Ayati, S. Mirzaei, Comparative study of metal nanoparticles anchored TiO2 using polyoxometalate intermediate in photodegradation of azo dye pollutant in aquatic environments, Inorg Chem Commun 160 (2024) 111986. https://doi.org/https://doi.org/10.1016/j.inoche.2023.111986.

[16] C. Awada, G. Barbillon, F. Charra, L. Douillard, J.J. Greffet, Experimental study of hot spots in gold/glass nanocomposite films by photoemission electron microscopy, Phys Rev B 85 (2012) 6. https://doi.org/10.1103/PhysRevB.85.045438.

[17] H.S. Lee, C. Awada, S. Boutami, F. Charra, L. Douillard, R.E. de Lamaestre, Loss mechanisms of surface plasmon polaritons propagating on a smooth polycrystalline Cu surface, Opt Express 20 (2012) 8974–8981. https://doi.org/10.1364/oe.20.008974.

[18] C. Awada, T. Popescu, L. Douillard, F. Charra, A. Perron, H. Yockell-Lelievre, A.L. Baudrion, P.M. Adam, R. Bachelot, Selective Excitation of Plasmon Resonances of Single Au Triangles by Polarization-Dependent Light Excitation, Journal of Physical Chemistry C 116 (2012) 14591–14598. https://doi.org/10.1021/jp303475c.

[19] D. Gogoi, A. Namdeo, A.K. Golder, N.R. Peela, Ag-doped TiO2 photocatalysts with effective charge transfer for highly efficient hydrogen production through water splitting, Int J Hydrogen Energy 45 (2020) 2729–2744. https://doi.org/https://doi.org/10.1016/j.ijhydene.2019.11.127.

[20] G. Kawamura, T. Arai, H. Muto, A. Matsuda, Charge behavior in a plasmonic photocatalyst composed of Au and TiO2, Catal. Sci. Technol. 8 (2018) 1813–1818. https://doi.org/10.1039/C8CY00120K.

[21] V. Etacheri, C. Di Valentin, J. Schneider, D. Bahnemann, S.C. Pillai, Visible-light activation of TiO2 photocatalysts: Advances in theory and experiments, Journal of Photochemistry and Photobiology C: Photochemistry Reviews 25 (2015) 1–29. https://doi.org/https://doi.org/10.1016/j.jphotochemrev.2015.08.003.

[22] R. Konta, T. Ishii, H. Kato, A. Kudo, Photocatalytic Activities of Noble Metal Ion Doped SrTiO3 under Visible Light Irradiation, J Phys Chem B 108 (2004) 8992–8995. https://doi.org/10.1021/jp049556p.

[23] A. Haruna, I. Abdulkadir, S.O. Idris, Photocatalytic activity and doping effects of BiFeO3 nanoparticles in model organic dyes, Heliyon 6 (2020) e03237. https://doi.org/https://doi.org/10.1016/j.heliyon.2020.e03237.

[24] M. Tahir, B. Tahir, N. Kumar, M. Al Marzooqi, M. Siraj, A. Fatehmulla, In-situ synthesis of V2AlC@V2O5/TiO2 immobilized over honeycomb support with vanadium oxide electron transfer mediator for stimulating selective CO2 photoreduction through bi-reforming in a monolith reactor, Fuel 370 (2024) 131816. https://doi.org/https://doi.org/10.1016/j.fuel.2024.131816.

[25] V. Soni, Sonu, P. Singh, S. Thakur, T. Ahamad, V.-H. Nguyen, V. Chaudhary, N. Kumar, S. Kaya, C.M. Hussain, P. Raizada, Oxygen vacancy enriched SrTiO3 and NiO-based S-scheme heterojunction moored on activated carbon from exhausted water filter batteries for ameliorated photodegradation of doxycycline hydrochloride and methyl orange degradation, J Taiwan Inst Chem Eng 159 (2024) 105419. https://doi.org/https://doi.org/10.1016/j.jtice.2024.105419.

[26] A. Sharma, A. Mittal, S. Sharma, M. Tahir, D. Parmar, P. Singh, N. Kumar, Integrating Ni, Pt, and Pd on Biphasic Cu-Doped Bi2O3 for Physicochemical Characteristics and Superior Light Driven Elimination of Pollutants, Catalysis Surveys from Asia 28 (2024) 101–116. https://doi.org/10.1007/s10563-023-09411-0.

[27] J. Saroha, E. Rani, M. Devi, P. Pathi, M. Kumar, S.N. Sharma, Plasmon-assisted photocatalysis of organic pollutants by Au/Ag–TiO2 nanocomposites: a comparative study, Materials Today Sustainability 23 (2023) 100466. https://doi.org/https://doi.org/10.1016/j.mtsust.2023.100466.

[28] I.S. Saputra, Y. Yulizar, R.P. Arindra, D. Annas, K.C. Sembiring, Sudirman, Green Decorated of Au/TiO2 Nanocomposites as Superior Photocatalyst in Methylene Blue Dye Degradation Under Sodium Light Irradiation, Int J Environ Res 18 (2023) 8. https://doi.org/10.1007/s41742-023-00559-1.

[29] L. Du, A. Furube, K. Hara, R. Katoh, M. Tachiya, Ultrafast plasmon induced electron injection mechanism in gold–TiO2 nanoparticle system, Journal of Photochemistry and Photobiology C: Photochemistry Reviews 15 (2013) 21–30. https://doi.org/https://doi.org/10.1016/j.jphotochemrev.2012.11.001.

[30] H. Zhang, G. Wang, D. Chen, X. Lv, J. Li, Tuning Photoelectrochemical Performances of Ag−TiO2 Nanocomposites via Reduction/Oxidation of Ag, Chemistry of Materials 20 (2008) 6543–6549. https://doi.org/10.1021/cm801796q.

[31] I. Paramasivam, J.M. Macak, P. Schmuki, Photocatalytic activity of TiO2 nanotube layers loaded with Ag and Au nanoparticles, Electrochem Commun 10 (2008) 71–75. https://doi.org/10.1016/j.elecom.2007.11.001.

[32] L. Armelao, D. Barreca, G. Bottaro, S. Gross, A. Gasparotto, C. Maragno, E. Tondello, A. Zattin, Introduction to XPS Studies of Metal and Metal-oxide Nanosystems, Surface Science Spectra 10 (2003) 137–142. https://doi.org/10.1116/11.20050199.

[33] A. Sousa-Castillo, M. Comesaña-Hermo, B. Rodríguez-González, M. Pérez-Lorenzo, Z. Wang, X.-T. Kong, A.O. Govorov, M.A. Correa-Duarte, Boosting Hot Electron-Driven Photocatalysis through Anisotropic Plasmonic Nanoparticles with Hot Spots in Au–TiO2 Nanoarchitectures, The Journal of Physical Chemistry C 120 (2016) 11690–11699. https://doi.org/10.1021/acs.jpcc.6b02370.

[34] W.L. Barnes, A. Dereux, T.W. Ebbesen, Surface plasmon subwavelength optics, Nature 424 (2003) 824–830. https://doi.org/10.1038/nature01937.

[35] D.K. Gramotnev, S.I. Bozhevolnyi, Plasmonics beyond the diffraction limit, Nat Photonics 4 (2010) 83–91. https://doi.org/10.1038/nphoton.2009.282.

[36] H. Bin Jeon, P.V. Tsalu, J.W. Ha, Shape Effect on the Refractive Index Sensitivity at Localized Surface Plasmon Resonance Inflection Points of Single Gold Nanocubes with Vertices, Sci Rep 9 (2019) 13635. https://doi.org/10.1038/s41598-019-50032-3.

[37] X. Huang, M.A. El-Sayed, Gold nanoparticles: Optical properties and implementations in cancer diagnosis and photothermal therapy, J Adv Res 1 (2010) 13–28. https://doi.org/https://doi.org/10.1016/j.jare.2010.02.002.

[38] S. V Sheen Mers, S. Umadevi, V. Ganesh, Controlled Growth of Gold Nanostars: Effect of Spike Length on SERS Signal Enhancement, ChemPhysChem 18 (2017) 1358–1369. https://doi.org/10.1002/cphc.201601380.

[39] N. Schwenk, B. Mizaikoff, S. Cárdenas, Á.I. López-Lorente, Gold-nanostar-based SERS substrates for studying protein aggregation processes, Analyst 143 (2018) 5103–5111. https://doi.org/10.1039/C8AN00804C.

[40] T. Sen, G. Kaur, S. Tanwar, V. Kaur, R. Biswas, S. Saini, K. kanta Haldar, Interfacial design of gold/silver core-shell nanostars for plasmon enhanced photocatalytic coupling of 4-aminothiophenol, J. Mater. Chem. C (2021). https://doi.org/10.1039/D1TC03733A.

[41] A.I. Hochbaum, R. Chen, R.D. Delgado, W. Liang, E.C. Garnett, M. Najarian, A. Majumdar, P. Yang, Enhanced thermoelectric performance of rough silicon nanowires, Nature 451 (2008) 163–167. https://doi.org/10.1038/nature06381.

[42] B. Bhowmik, K. Dutta, N. Banerjee, A. Hazra, P. Bhattacharyya, Low temperature acetone sensor based on Sol-gel grown nano TiO<inf>2</inf> thin film, in: 2013 IEEE International Conference ON Emerging Trends in Computing, Communication and Nanotechnology (ICECCN), IEEE, 2013: pp. 553–557. https://doi.org/10.1109/ICE-CCN.2013.6528561.

[43] A. Subrahmanyam, B. KP, P. Rajesh, K. KJ, K. MR, Surface modification of sol gel TiO2 surface with sputtered metallic silver for Sun light photocatalytic activity: Initial studies, Solar Energy Materials and Solar Cells 101 (2012) 241–248. https://doi.org/10.1016/j.solmat.2012.01.023.

[44] Z. Wei, R. Li, T. Huang, A. Yu, Fabrication of morphology controllable rutile TiO2 nanowire arrays by solvothermal route for dye-sensitized solar cells, Electrochim Acta 56 (2011) 7696–7702. https://doi.org/https://doi.org/10.1016/j.electacta.2011.06.038.

[45] R.J. Tayade, R.G. Kulkarni, Raksh. V Jasra, Transition Metal Ion Impregnated Mesoporous TiO2 for Photocatalytic Degradation of Organic Contaminants in Water, Ind Eng Chem Res 45 (2006) 5231–5238. https://doi.org/10.1021/ie051362o.

[46] M. Kanoun, C. Awada, F. ahmed, C. Jonin, P. F. Brevet, Band gap engineering of Au doping and Au – N codoping into anatase TiO2 for enhancing the visible light photocatalytic performance, Int J Hydrogen Energy HE-D-23-01 (2023) 1–7. https://doi.org/HE-D-23-01603R2.

[47] F. Ahmed, M.B. Kanoun, C. Awada, C. Jonin, P.-F. Brevet, An Experimental and Theoretical Study on the Effect of Silver Nanoparticles Concentration on the Structural, Morphological, Optical, and Electronic Properties of TiO2 Nanocrystals, Crystals (Basel) 11 (2021). https://doi.org/10.3390/cryst11121488.

[48] J.D. Park, B.H. Son, J.K. Park, S.Y. Kim, J.-Y. Park, S. Lee, Y.H. Ahn, Diffusion length in nanoporous TiO2 films under above-band-gap illumination, AIP Adv 4 (2014) 67106. https://doi.org/10.1063/1.4881875.

[49] G.D. Venkatasubbu, V. Ramakrishnan, V. Sasirekha, S. Ramasamy, J. Kumar, Influence of particle size on the phonon confinement of TiO2 nanoparticles, J Exp Nanosci 9 (2014) 661–668. https://doi.org/10.1080/17458080.2012.689018.

[50] J. Schneider, M. Matsuoka, M. Takeuchi, J. Zhang, Y. Horiuchi, M. Anpo, D.W. Bahnemann, Understanding TiO2 Photocatalysis: Mechanisms and Materials, Chem Rev 114 (2014) 9919–9986. https://doi.org/10.1021/cr5001892.

[51] P.P. Lottici, D. Bersani, M. Braghini, A. Montenero, Raman scattering characterization of gel-derived titania glass, J Mater Sci 28 (1993) 177–183. https://doi.org/10.1007/BF00349049.

[52] R.G. Toro, M. Diab, T. de Caro, M. Al-Shemy, A. Adel, D. Caschera, Study of the Effect of Titanium Dioxide Hydrosol on the Photocatalytic and Mechanical Properties of Paper Sheets, Materials 13 (2020). https://doi.org/10.3390/ma13061326.

[53] X.-F. Wu, H.-Y. Song, J.-M. Yoon, Y.-T. Yu, Y.-F. Chen, Synthesis of Core−Shell Au@TiO2 Nanoparticles with Truncated Wedge-Shaped Morphology and Their Photocatalytic Properties, Langmuir 25 (2009) 6438–6447. https://doi.org/10.1021/la900035a.

[54] J.-J. Chen, J.C.S. Wu, P.C. Wu, D.P. Tsai, Improved Photocatalytic Activity of Shell-Isolated Plasmonic Photocatalyst Au@SiO2/TiO2 by Promoted LSPR, The Journal of Physical Chemistry C 116 (2012) 26535–26542. https://doi.org/10.1021/jp309901y.

[55] P. Birnal, M.C. Marco de Lucas, I. Pochard, F. Herbst, O. Heintz, L. Saviot, B. Domenichini, L. Imhoff, Visible-light photocatalytic degradation of dyes by TiO2–Au inverse opal films synthesized by Atomic Layer Deposition, Appl Surf Sci 609 (2023) 155213. https://doi.org/https://doi.org/10.1016/j.apsusc.2022.155213.

[56] B. Yaou Balarabe, P. Maity, A polymer-Au/TiO2 nano-composite based floating catalyst for photocatalytic dye degradation under natural sunlight, J Photochem Photobiol A

Chem 449 (2024) 115405. https://doi.org/https://doi.org/10.1016/j.jphotochem.2023.115405.

[57] M. Alsaidi, F.A. Azeez, L.A. Al-Hajji, A.A. Ismail, Hierarchical porous TiO2 with a uniform distribution of anchored gold nanoparticles for enhanced photocatalytic efficiency and accelerated charge separation for the degradation of antibiotics, Environmental Science and Pollution Research 30 (2023) 17951–17964. https://doi.org/10.1007/s11356-022-23249-5.

[58] W. Qi, M. Wang, Y. Su, Size effect on the lattice parameters of nanoparticles, Journal of Materials Science Letters - J MATER SCI LETT 21 (2002) 877–878. https://doi.org/10.1023/A:1015778729898.

[59] M.N. Ghazzal, N. Chaoui, M. Genet, E.M. Gaigneaux, D. Robert, Effect of compressive stress inducing a band gap narrowing on the photoinduced activities of sol–gel TiO2 films, Thin Solid Films 520 (2011) 1147–1154. https://doi.org/https://doi.org/10.1016/j.tsf.2011.08.097.

[60] H. Wang, T. You, W. Shi, J. Li, L. Guo, Au/TiO2/Au as a Plasmonic Coupling Photocatalyst, The Journal of Physical Chemistry C 116 (2012) 6490–6494. https://doi.org/10.1021/jp212303q.

[61] L.-P. Wu, W.-G. Wang, D. Mo, J.-L. Duan, X.-J. Li, Effect of Au position on the photoelectrochemical and photocatalytic activity of TiO2 nanotubes under UV irradiation, Inorganic and Nano-Metal Chemistry (n.d.) 1–9. https://doi.org/10.1080/24701556.2023.2166067.

[62] L. Wu, S. Ma, P. Chen, X. Li, The mechanism of enhanced charge separation and photocatalytic activity for Au@TiO2 core-shell nanocomposite, Int J Environ Anal Chem 103 (2023) 201–211. https://doi.org/10.1080/03067319.2020.1855337.

[63] X. Yang, Y. Wang, L. Zhang, H. Fu, P. He, D. Han, T. Lawson, X. An, The Use of Tunable Optical Absorption Plasmonic Au and Ag Decorated TiO2 Structures as Efficient Visible Light Photocatalysts, Catalysts 10 (2020). https://doi.org/10.3390/catal10010139.

[64] M. Jakob, H. Levanon, P. V Kamat, Charge Distribution between UV-Irradiated TiO2 and Gold Nanoparticles: Determination of Shift in the Fermi Level, Nano Lett 3 (2003) 353–358.

[65] A.A. Melvin, K. Illath, T. Das, T. Raja, S. Bhattacharyya, C.S. Gopinath, M–Au/TiO2 (M = Ag, Pd, and Pt) nanophotocatalyst for overall solar water splitting: role of interfaces, Nanoscale 7 (2015) 13477–13488. https://doi.org/10.1039/C5NR03735B.

[66] G.D. Venkatasubbu, V. Ramakrishnan, V. Sasirekha, S. Ramasamy, J. Kumar, Influence of particle size on the phonon confinement of TiO2 nanoparticles, J Exp Nanosci 9 (2014) 661–668. https://doi.org/10.1080/17458080.2012.689018.

[67] O. Saber, H. Alomair, M. Abu-Abdeen, A. Aljaafari, Fast Degradation of Green Pollutants Through Nanonets and Nanofibers of the Al-Doped Zinc Oxide, Acta Metallurgica Sinica (English Letters) 31 (2018) 533–546. https://doi.org/10.1007/s40195-017-0682-4.

[68] G. Wan, X. Peng, M. Zeng, L. Yu, K. Wang, X. Li, G. Wang, The Preparation of Au@TiO2 Yolk–Shell Nanostructure and its Applications for Degradation and Detection of Methylene Blue, Nanoscale Res Lett 12 (2017) 535. https://doi.org/10.1186/s11671-017-2313-4.

[69] F. Shan, T. Zhang, Theoretical study on surface plasmon properties of gold nanostars, IOP Conf Ser Mater Sci Eng 322 (2018) 022005. https://doi.org/10.1088/1757-899X/322/2/022005.

[70] H. Chen, G. Liu, L. Wang, Switched photocurrent direction in Au/TiO2 bilayer thin films, Sci Rep 5 (2015) 10852. https://doi.org/10.1038/srep10852.

[71] O. Saber, H.M. Kotb, M. Osama, H.A. Khater, An Effective Photocatalytic Degradation of Industrial Pollutants through Converting Titanium Oxide to Magnetic Nanotubes and Hollow Nanorods by Kirkendall Effect., Nanomaterials (Basel) 12 (2022). https://doi.org/10.3390/nano12030440.

[72] F. Azeez, E. Al-Hetlani, M. Arafa, Y. Abdelmonem, A.A. Nazeer, M.O. Amin, M. Madkour, The effect of surface charge on photocatalytic degradation of methylene blue dye using chargeable titania nanoparticles, Sci Rep 8 (2018) 7104. https://doi.org/10.1038/s41598-018-25673-5.

[73] L.M. Santos, W.A. Machado, M.D. França, K.A. Borges, R.M. Paniago, A.O.T. Patrocinio, A.E.H. Machado, Structural characterization of Ag-doped TiO2 with enhanced photocatalytic activity, RSC Adv. 5 (2015) 103752–103759. https://doi.org/10.1039/C5RA22647C.

[74] S.B. Khan, M. Hou, S. Shuang, Z. Zhang, Morphological influence of TiO2 nanostructures (nanozigzag, nanohelics and nanorod) on photocatalytic degradation of organic dyes, Appl Surf Sci 400 (2017) 184–193. https://doi.org/https://doi.org/10.1016/j.apsusc.2016.12.172.

[75] N. Al Suliman, C. Awada, A. Alshoaibi, N.M. Shaalan, Simple Preparation of Ceramic-Like Materials Based on 1D-Agx(x=0, 5, 10, 20, 40 mM)/TiO2 Nanostructures and Their Photocatalysis Performance, Crystals (Basel) 10 (2020). https://doi.org/10.3390/cryst10111024.

[76] S. Smidstrup, T. Markussen, P. Vancraeyveld, J. Wellendorff, J. Schneider, T. Gunst, B. Verstichel, D. Stradi, P.A. Khomyakov, U.G. Vej-Hansen, M.-E. Lee, S.T. Chill, F. Rasmussen, G. Penazzi, F. Corsetti, A. Ojanperä, K. Jensen, M.L.N. Palsgaard, U. Martinez, A. Blom, M. Brandbyge, K. Stokbro, {QuantumATK}: an integrated platform of electronic and atomic-scale modelling tools, Journal of Physics: Condensed Matter 32 (2019) 15901. https://doi.org/10.1088/1361-648x/ab4007.

[77] J.P. Perdew, K. Burke, M. Ernzerhof, Generalized Gradient Approximation Made Simple [Phys. Rev. Lett. 77, 3865 (1996)], Phys. Rev. Lett. 78 (1997) 1396. https://doi.org/10.1103/PhysRevLett.78.1396.

[78] A.Yu. Tsivadze, G. V Ionova, V.K. Mikhalko, I.S. Ionova, G.A. Gerasimova, Plasmon properties of silver spherical nanoparticles and films, Protection of Metals and Physical Chemistry of Surfaces 49 (2013) 169–172. https://doi.org/10.1134/S207020511302010X.

[79] E. Mete, O. Gülseren, Ş. Ellialtıoğlu, Modification of ${\text{TiO}}_{2}(001)$ surface electronic structure by Au impurity investigated with density functional theory, Phys Rev B 80 (2009) 35422. https://doi.org/10.1103/PhysRevB.80.035422.

[80] F. Ahmed, M.B. Kanoun, C. Awada, C. Jonin, P.-F. Brevet, An Experimental and Theoretical Study on the Effect of Silver Nanoparticles Concentration on the Structural, Morphological, Optical, and Electronic Properties of TiO2 Nanocrystals, Crystals (Basel) 11 (2021). https://doi.org/10.3390/cryst11121488.

[81] S. Wang, C. Ren, H. Tian, J. Yu, M. Sun, MoS2/ZnO van der Waals heterostructure as a high-efficiency water splitting photocatalyst: a first-principles study, Phys. Chem. Chem. Phys. 20 (2018) 13394–13399. https://doi.org/10.1039/C8CP00808F.

[82] X. Huang, X. Shu, J. Li, Z. Cui, S. Cao, W. Chen, J. Yin, G. Yan, H. Zhao, J. Hu, Z. Yang, Y. Wang, DFT study on type-II photocatalyst for overall water splitting: g-GaN/C2N van der Waals heterostructure, Int J Hydrogen Energy 48 (2023) 12364–12373. https://doi.org/https://doi.org/10.1016/j.ijhydene.2022.12.146.

[83] N. Shahzad, A. Hussain, N. Mustafa, N. Ali, M.B. Kanoun, S. Goumri-Said, First principles study of the adsorption and dissociation mechanisms of H2S on a TiO2 anatase (001) surface, RSC Adv. 6 (2016) 7941–7949. https://doi.org/10.1039/C5RA20875K.

[84] M. Ikram, R. Raees, A. Haider, A. Ul-Hamid, J. Haider, I. Shahzadi, W. Nabgan, S. Goumri-Said, M.B. Kanoun, S. Ali, Enhanced photocatalytic and antibacterial activity of TiO2 Quantum dots doped with Cerium/Chitosan for Environmental Remediation: Experimental and theoretical approaches, Mater Chem Phys 297 (2023) 127462. https://doi.org/https://doi.org/10.1016/j.matchemphys.2023.127462.